Euler Analysis of a High-Speed Civil Transport Concept at Mach 3

James L. Pittman* and Daryl L. Bonhaus†
NASA Langley Research Center, Hampton, Virginia 23665
Michael J. Siclari‡
Grumman Aerospace Corporation, Bethpage, New York 11714
and
Samuel M. Dollyhigh§
NASA Langley Research Center, Hampton, Virginia 23665

A marching Euler solver, GEM3D, was used to predict the Mach 3 flowfield for the wing and body of a High-Speed Civil Transport (HSCT) concept. The analysis focused on a typical cruise lift coefficient of 0.1 at $\alpha = 3$ deg. The Euler solution indicated that embedded shocks formed on the upper surface of the inboard wing panel and at the leading edge of the outboard wing panel caused by its supersonic leading-edge condition. According to a simple static-pressure criterion, the embedded wing upper-surface shocks were sufficiently strong to separate a turbulent boundary layer. Comparison of aerodynamic coefficients from the Euler solver with those from linear theory showed that the linear theory estimates of lift and drag were optimistic, which would lead to optimistic estimates of cruise range.

Nomenclature

C_D = drag coefficient
C_L = lift coefficient
C_m = pitching-moment coefficient
C_p = pressure coefficient
I = number of circumferential grid points on the half-body
J = number of radial grid points
L/D = lift-to-drag ratio
M = freestream Mach number
R = spherical radius, ft
x = aircraft longitudinal coordinate (Fig. 1), ft
y = aircraft spanwise coordinate (Fig.1), ft
z = aircraft vertical coordinate, ft
α = angle of attack, deg
β = $(M^2-1)^{1/2}$
Λ = wing leading-edge sweep angle, deg

Subscript
LE = leading edge

Introduction

THERE has been a resurgence of interest in high-speed aircraft in the United States in the last few years. A major research and development effort is currently focused on the National Aero-Space Plane (NASP) Project, which is planned to demonstrate a single-stage-to-orbit capability using air breathing propulsion.[1] Another major national research effort is the High-Speed Civil Transport (HSCT) Program, which focuses on the technology to design a commercially viable supersonic transport.[2,3]

NASA Langley Research Center is conducting in-house HSCT studies, in addition to contractual studies at Boeing and McDonnell-Douglas. One particular NASA Langley HSCT study has defined an advanced Mach 3 cruise transport concept,[4] which is the configuration of interest for this investigation. This concept was sized to carry 250 passengers for 6500 n. mi. The conceptual design study includes inputs from the discipline areas of aerodynamics, structures, materials, propulsion, and acoustics, as well as economic studies that assess the costs and benefits of technologies from each discipline.

The NASA Langley design study has concentrated primarily on the cruise and landing conditions, using linearized potential theory methodology to define the vehicle shape and to predict aerodynamic quantities. This technology is mature, widely used, and entirely adequate for the conceptual and preliminary design levels. However, it is largely unchanged from that described by Baals et al.[5] and Kulfan and Sigalla[6] in publications dated 1968 and 1978, respectively. Consequently, improvements in the aerodynamic performance of supersonic transports are most likely to be obtained through the application of more accurate computational fluid dynamics (CFD) methods, which have become viable research tools in the last decade. Therefore, the objective of this paper is to demonstrate the first step in that process of applying CFD methods in the HSCT aircraft design process: the Euler analysis of the wing and body of a Mach 3 HSCT at its cruise condition.

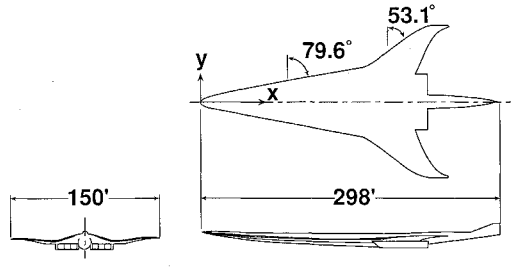

Fig. 1 Three-view drawing of a Mach 3 cruise HSCT concept.

Presented as Paper 89-2174 at the AIAA 7th Applied Aerodynamics Conference, Seattle, WA, July 31–Aug. 2, 1989; received Aug. 26, 1989; revision received Feb. 28, 1990; accepted for publication Aug. 3, 1990.

*Assistant Head, Aerothermal Loads Branch, Structural Mechanics Division. Associate Fellow AIAA.
†Aerospace Engineer, Computational Aerodynamics Branch, Fluid Mechanics Division. Member AIAA.
‡Senior Research Scientist. Associate Follow AIAA.
§Head, Systems Analysis Branch, Advanced Vehicles Division. Associate Fellow AIAA.

Concept Description

A three-view drawing of the Mach 3 HSCT concept is given in Fig. 1. It is a blended wing-body configuration with a modified platypus nose, a 79.6-deg swept inboard wing panel, a 53.1-deg swept outboard wing panel, and curved wingtips. The wing planform was selected to minimize induced drag and wave drag due to lift while maintaining adequate low-speed characteristics. This planform also minimizes the shift of the aerodynamic center between landing and cruise conditions. The platypus nose is designed to minimize sonic boom, lower volumetric wave drag, and improve low-speed lateral-directional aerodynamic characteristics.

The inboard wing panel has a subsonic leading edge at the cruise Mach number. The value of the linear theory similarity parameter, $\beta \cot\Lambda$, is 0.52. The high sweep angle allows a blunt leading edge without a wave drag penalty and an optimum cruise camber surface that is relatively insensitive to supersonic Mach number. The wing thickness ratio varies from 2% inboard to 4% at the intersection of the inboard and outboard wing panels.

The outboard wing panel has a supersonic leading edge at Mach 3. The value of $\beta \cot\Lambda$ is 2.12. The outboard wing panel features a nearly zero leading-edge radius to reduce wave drag and is uncambered. The outboard wing panel has a thickness ratio of about 4%. The curved wingtip is designed to control pitchup problems for subsonic, high-α conditions.

Euler Computational Method

The Euler solver used for this study is referred to as GEM3D[7] and solves the three-dimensional unsteady Euler equations for a supersonic or hypersonic flow. The Euler equations are written in conservation form in a spherical coordinate system. The initial solution is obtained on a conical nose cap, and the fully three-dimensional solution is determined by marching down the length of the body on spherical planes. A fully converged solution is computed on each crossflow plane before marching to the next crossflow plane. All shocks are captured in the grid.

The numerical scheme for the crossflow planes is a node-centered, physical space, finite-volume, central difference scheme. The node-centered scheme eliminates the need to extrapolate the pressure terms to the boundary. The steady-state solution is obtained by an explicit pseudotime Runge-Kutta integration. Local time stepping and implicit residual smoothing are used to accelerate solution convergence in each crossflow plane. Fourth-order explicit artificial viscosity is added for solution stability, and second-order explicit artificial viscosity is added to damp oscillations near shocks. The second-order artificial viscosity is proportional to the pressure gradient across the shock.

The numerical scheme in the marching direction is an implicit upwind finite-difference technique. The upwind treatment of the marching terms eliminates the need for explicit artificial viscosity in the marching direction. Marching on spherical planes is advantageous at lower supersonic Mach numbers compared to marching on Cartesian planes because of the requirement that the flow be fully supersonic in the marching direction at all points.

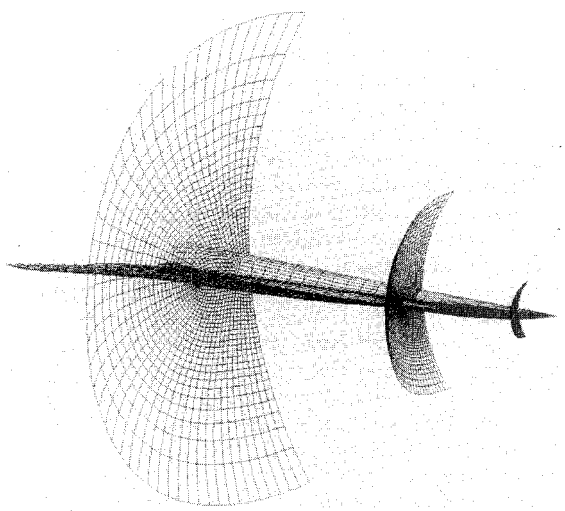

Fig. 2 Typical spherical marching planes for HSCT wing body.

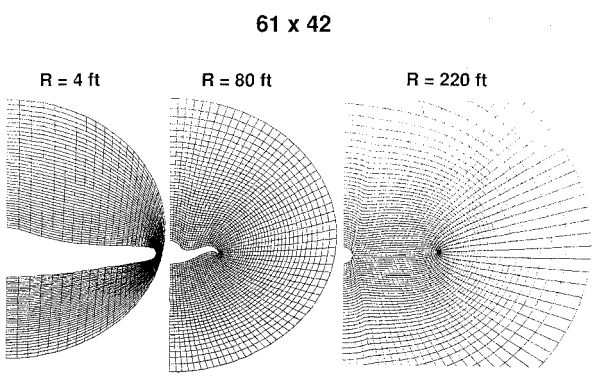

Fig. 3 Crossplane grids (61 × 42) at R = 4, 80, and 220 ft.

Grid Density Study

The effect of grid density on the resolution of the flowfield can be determined using aerodynamic parameters. The inviscid drag coefficient is a key aerodynamic parameter, especially for long range transport aircraft, and was used as the quantitative figure of merit in the grid density study. The three-dimensional grid can be decomposed into a two-dimensional crossplane grid and the marching step size which is the distance between crossplane grids.

Crossplane grid densities can be expressed as $I \times J$, where the first integer specifies the number of points around the half-body, and the second integer specifies the number of points from the inner boundary (the body surface) to the outer boundary, with the restriction that the outer boundary fall outside of the bow shock. A cosine function clusters the circumferential points near the leading edge, and an exponential function clusters the body-normal points near the body. To maintain solution accuracy, it is necessary to increase the grid stretching down the length of the body because of the expansion of the crossplane grids. The expansion of the spherical crossplane grids with increasing longitudinal distance is illustrated in Fig. 2.

Crossplane grid densities of 61 × 42 and 97 × 58 were investigated for a nominal step size of 4 ft. The final solution plane is at R = 264 ft, which is the approximate location of the wingtip trailing edge, yielding roughly 180,000 and 394,000 grid points, respectively. Crossplane grids at R = 4, 80, and 220 ft for a 61 × 42 grid are presented in Fig. 3. The grid at R = 220 ft includes a thin wing segment, a portion of the wake, and the body extension into the wake region.

Solutions for both crossplane grid densities for several α from 0–6 deg were obtained at Mach 3. The 97 × 58 grid provided a slightly sharper resolution of shocks, as expected, but the integrated longitudinal forces and pitching moment do not change appreciably for these two grids. The inviscid drag coefficient for the 97 × 58 grid runs is consistently about 1 count lower than for the 61 × 42 grid across this α range because of improved resolution of the expansion pressure on the leading edge for the 97 × 58 grid. One drag count is approximately 1% of the inviscid drag at the cruise point, α = 3 deg. The 61 × 42 grid solutions require approximately 11–12 min of CRAY-2 time; the 97 × 58 grid solutions require approximately 30 min.

Solutions for a variation of marching step size were obtained for the 61 × 42 crossplane grid. In addition to the original 4-ft step size, a nominal step size of 2 ft was investigated, which yields about 343,000 total grid points. A 4-ft marching

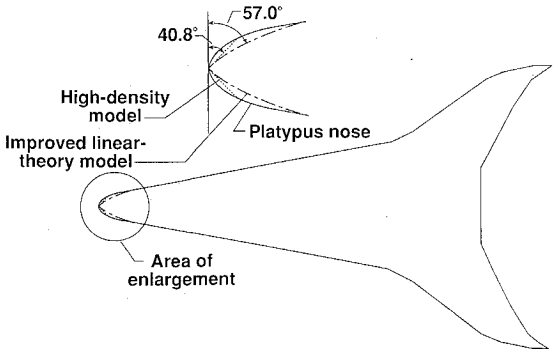

Fig. 4 Planform comparison: concept, high-density numerical model, and improved linear theory numerical model.

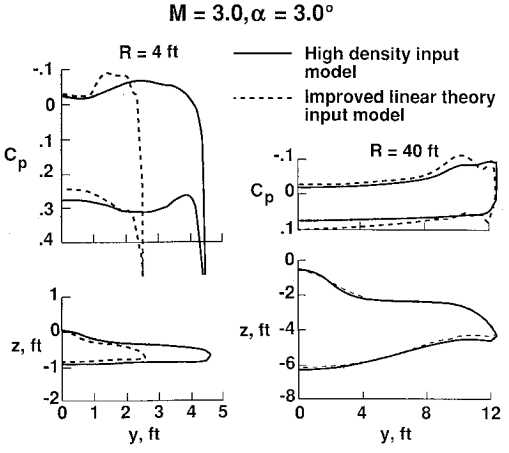

Fig. 5 Comparison of Euler predictions using the high-density and improved linear theory input models, $M = 3.0$, $\alpha = 3.0$ deg.

step size is approximately 1.5% of the total length. The effect of this reduction in step size on the integrated forces and moments was also small. For example, the inviscid drag coefficient from this series of runs at Mach 3 was consistently higher than those from the 4-ft step size runs. At $\alpha = 0$ deg, the increase was about 0.5 drag counts, increasing to about 2 counts at $\alpha = 6$ deg. CRAY-2 run times for these cases were roughly 25 min.

A converged solution is obtained when the maximum residual for all five governing equations is reduced below 0.01. Numerical experiments performed on the 61 × 42 crossplane grid and a 4-ft marching step size determined that reducing the maximum residual by an additional factor of 10 did not appreciably change the surface pressure distribution. The change in the integrated inviscid drag coefficient was less than 0.00001 or 0.1 drag count at $M = 3$, $\alpha = 3.0$ deg.

Numerical Input Models

The numerical model used to perform linear theory calculations for the design study[4] was modified for use in GEM3D. Linear theory methods can obtain solutions using relatively sparse input models, but the geometry requirements for CFD methods are more stringent. The same geometry input format[8] was used for both the linear theory calculations and the GEM3D calculations. This input format defines the body as cross sections and the wing as streamwise chords. More than two man-months were required to refine the original input model to obtain a GEM3D solution.

The refinement of the input model involved graphically displaying cross sections of the geometry, curve fitting the points, and interpolating to obtain a sufficient number of input points using the GEOM[9] software. A sufficient number of input points is defined by achieving a good solution at each cross section. The complex curved surfaces of the geometry significantly increased the difficulty of this task, particularly for the nose region, the inboard wing leading edge, and the intersecting chord of the wing and body. The original input model contained less than 1000 points and the new numerical input model, which is referred to as the improved linear theory model, contained approximately 2500 points.

As the in-house HSCT studies continued to evolve at Langley, a wind-tunnel model of the Mach 3 concept was designed to verify predicted performance levels and to provide data for future code validation studies. A new high-density numerical model containing approximately 7500 surface points was defined from the wind-tunnel model data base. For this numerical model, the entire wing and body were specified as cross sections to avoid inaccuracies when merging the wing and body.

The planform of the platypus nose concept is presented in Fig. 4, along with the planforms of the improved linear theory numerical model and the high-density numerical model. The platypus nose should be analyzed with a blunt body solver, even though the profile of the nose is extremely thin (see Fig. 1). However, a conical approximation for this nose shape yields a faster solution and is considered to be reasonable for the purpose of this paper. The initial leading-edge sweep angle of the high-density model is 40.8 deg, which is the minimum for an attached conical shock wave at Mach 3.[10] The initial leading-edge sweep angle of the improved linear-theory model is 57.0 deg. Although the overall difference in the planforms is confimed to the nose region, this difference is important because the initial flowfield influences all downstream flowfields.

A comparison of results from GEM3D using both numerical models as input is presented in Fig. 5. The calculation was performed at $M = 3$, $\alpha = 3$ deg for a 61 × 42 grid and a nominal 4-ft step size. The cross section of each model and the corresponding surface-pressure distribution at $R = 4$ and 40 ft are shown. At $R = 4$ ft, the cross section of the high-density model has nearly twice the span of that of the improved linear theory model, as well as larger centerline compression angles. The surface-pressure distributions are similar in character, but

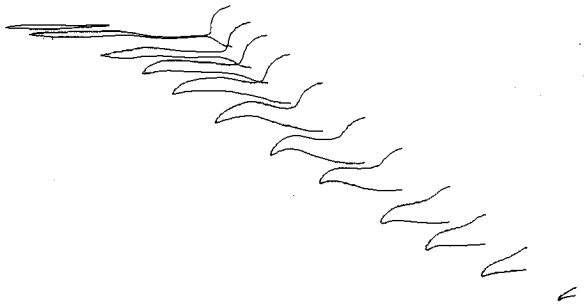

Fig. 6 Spherical cross sections of the HSCT wing body.

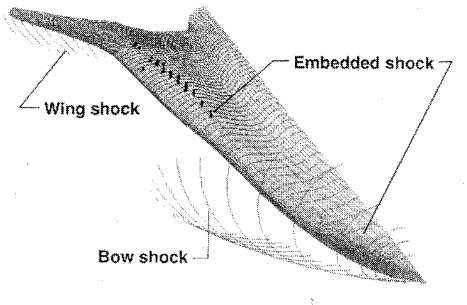

Fig. 7 Oblique view of Euler computed shock locations, $M = 3.0$, $\alpha = 3.0$ deg.

a slightly higher pressure is noted on the lower centerline for the high-density model and a strong crossflow shock develops on the upper surface of the improved linear theory model. The static pressure rise across the shock is 1.67, which is sufficiently strong to separate a turbulent boundary layer according to a criterion established for skewed shocks.[11] This criterion was recently validated for a crossflow shock wave that formed on a highly swept wing/body at $M = 1.6$ at high α.[12]

The cross sections of the two numerical models are nearly identical at $R = 40$ ft, but the pressure distributions are significantly different because of the different initial flowfields established in the nose region. These differences persist down the length of the inboard wing panel but diminish once the outboard wing panel emerges. The inviscid drag coefficient for the improved linear theory model is nearly 4 counts higher compared to that of the high-density model at $\alpha = 3$ deg. The stronger crossflow shock on the improved linear theory model is probably the cause of the increased drag.

Flowfield Analysis

An Euler analysis of the HSCT wing-body geometry will provide insight into the structure of the flowfield that cannot be obtained from linear theory. Euler methods accurately compute shock formations and surface pressures for attached flows. It is assumed that changes to the surface pressure caused by the boundary layer are negligibly small for moderate supersonic Mach number and low angle of attack.

The results are computed with GEM3D at a typical cruise condition of $M = 3$, $\alpha = 3$ deg for which the computed lift coefficient is roughly 0.1. The high-density numerical model is used exclusively for the Euler computations in the remainder of this paper. The grid is 97 × 58 for a 4-ft step size. Several spherical cross sections of the wing-body are shown in Fig. 6.

The formation of shocks in the flowfield can be visualized using a shock function algorithm found in the graphics package, PLOT3D. This algorithm searches the flowfield for sharp pressure gradients and then determines if the Mach number component across the pressure gradient changes from supersonic to subsonic. If so, a shock has been detected. As shown in Fig. 7, the results of this search of the Euler-computed flowfield clearly indicate the bow shock formed at the nose and the wing leading-edge shock on the outboard wing panel. These shocks diffuse at downstream locations because of the interaction of the shocks with expansion waves. Embedded crossflow shocks on the upper surface are also visible in the nose region and further down the inboard wing. The downstream embedded shocks occur near the maximum height of the curved wing surface.

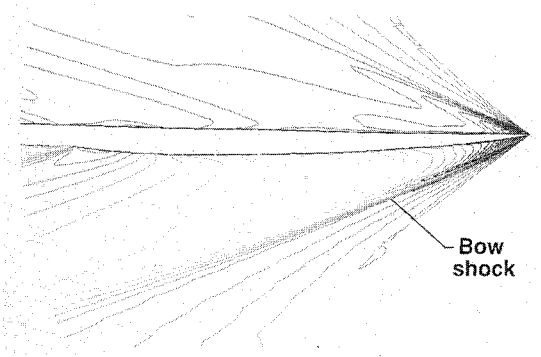

Fig. 8 Side view of Euler-computed centerline flowfield isoMachs, $M = 3.0$, $\alpha = 3.0$ deg.

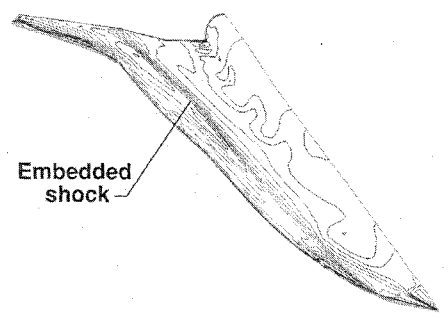

Fig. 9 Oblique view of upper surface isobars, $M = 3.0$, $\alpha = 3.0$ deg.

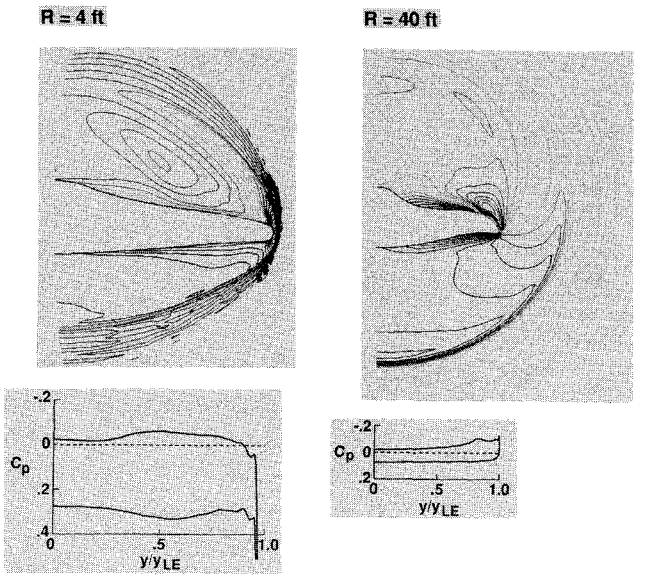

Fig. 10 Spherical cross section isoMachs, surface-pressure distribution at $M = 3.0$, $\alpha = 3.0$ deg for $R = 4$ and 40 ft.

The bow shock can be seen from another perspective, as shown in Fig. 8, where a side view of the centerline flowfield is presented. The clustered contour lines of constant Mach number indicate the location of the bow shock. The bow shock on the upper surface diffuses more quickly than on the lower surface because its initial strength is lower. The curved trajectory of the lower surface bow shock can be clearly seen.

The upper surface isobars are shown in Fig. 9. There is a region of large pressure gradients along the leading edge and a second region well inboard of the wing leading edge. The clustered leading-edge isobars indicate a rapid expansion and the inboard region of pressure gradients corresponds to the embedded shock locations noted on Fig. 7. The level of the upper surface pressure coefficient contour just inboard of the leading edge is roughly -0.1, which is approximately 63% of the vacuum pressure coefficient at Mach 3. The upper surface pressures continue to expand to levels as high as 80% of vacuum pressure before compressing.

The next three figures present flowfield contours of Mach number at selected spherical stations, under which is shown the surface-pressure distribution. Stations $R = 4$ and 40 ft are shown in Fig. 10. The blunt leading edge at $R = 4$ ft and the bow shock are clearly seen. The shock function algorithm indicates that an embedded shock forms above the body near the three closed Mach contours but does not extend down to the body surface. The surface-pressure distribution indicates a relatively mild recompression on the upper surface. At $R = 40$ ft, the leading edge is still rather blunt, but the bow shock is well away from the body. Note that the surface pressure on the lower surface has significantly decreased from $R = 4$ ft. A relatively weak shock forms on the upper surface at about 80% of semispan, but the shock strength is slightly less than that required to separate a turbulent boundary layer.

The data for stations $R = 80$ and 160 ft are shown in Fig. 11. $R = 80$ ft is roughly half the length of the inboard wing, and $R = 160$ ft is slightly upstream of the wing planform break. At $R = 80$ ft, the bow shock weakens and continues to move away from the body. The wing is highly cambered and

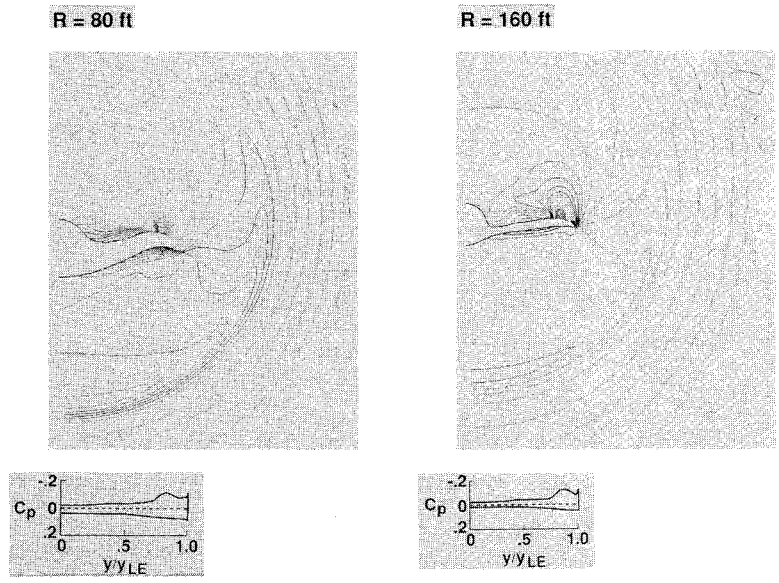

Fig. 11 Spherical cross section isoMachs, surface-pressure distribution at $M = 3.0$, $\alpha = 3.0$ deg for $R = 80$ and 160 ft.

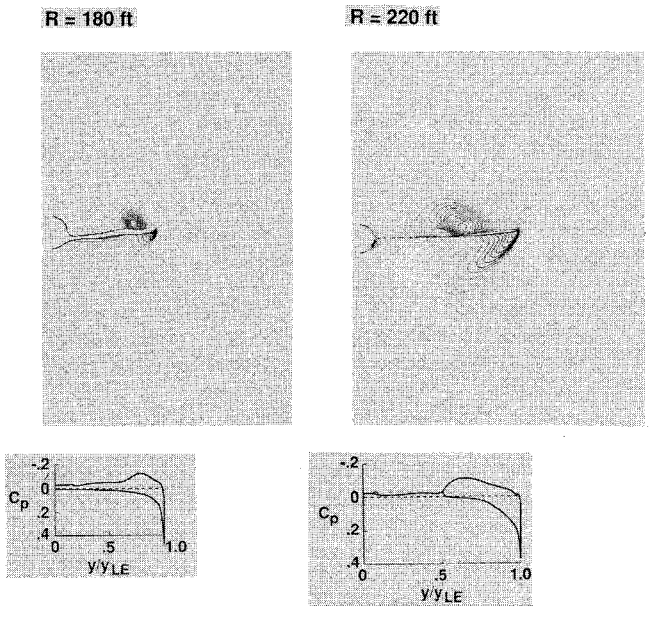

Fig. 12 Spherical cross section isoMachs, surface-pressure distribution at $M = 3.0$, $\alpha = 3.0$ deg for $R = 180$ and 220 ft.

the Mach number gradients near the wing surface are large. The flow expands around the leading edge onto the upper surface and decelerates through a crossflow shock to lower Mach numbers near the maximum height of the wing. The upper surface crossflow shock is indicated in the surface-pressure distribution. The static-pressure ratio, or strength, of this shock is estimated as 1.75 by the Euler method. This is greater than the necessary ratio of 1.5 for a skewed shock to separate a turbulent boundary layer. The wing geometry at $R = 160$ ft does not have the large leading-edge camber found at $R = 80$ ft because the geometry is transitioning to the uncambered outboard wing panel (53.1-deg sweep). However, the embedded shock is still evident, and its strength has increased to approximately 2.8.

The data for stations $R = 180$ and 220 ft are presented in Fig. 12. The forward station is located downstream of the planform break from the highly swept inboard panel to the supersonic leading-edge outboard panel. As noted in Fig. 7, a new shock forms on the outboard wing panel; this is also indicated by the large number of closely spaced isoMachs emanating downward from the sharp wing leading edge. The flow expands around the wing leading edge onto the upper surface and then compresses at about 70% semispan where the upper surface slopes downward. The static pressure rise across this shock is about 2.3. The station at $R = 220$ ft includes part of the wing, the wake, and the extension of the body into the wake region. The wing leading-edge shock is again clearly evident in the isoMachs, and surface-pressure contours show the formation of a trailing-edge shock. The trailing-edge shock strength is about 2.1. The surface-pressure distribution indicates there is no pressure rise across the wake, which is the correct condition.

Integrated Force Analysis

The ultimate measure of transport aircraft aerodynamic performance is the lift-to-drag ratio. The surface pressures computed from the GEM3D Euler method are integrated to determine the lift, drag, and pitching-moment coefficients. These coefficients are computed from solutions obtained with a 61 × 42 crossplane grid density and a nominal step size of 4 ft, using the high-density numerical input model. Experimental data are not available for this configuration, so comparisons are made with the linear theory results from the design study.[4] The area of surface-pressure integration does not include the body extension into the wake region for consistency with the linear theory aerodynamic coefficients. The planform shown on Fig. 4 indicates the area of integration.

The lift and pitching-moment coefficients are plotted vs α in Fig. 13. Two different linear theory estimates are shown: one from the classical linear method,[13,14] and another estimate that includes an increment for the attainable leading-edge thrust.[15] The Euler method predicts a slightly lower lift compared to the classical linear theory prediction. The attainable thrust estimate is identical to the classical no-thrust estimate until $\alpha \sim 2.5$ deg, at which point there is a lift increment due to attainable thrust. The pitching-moment comparison between the Euler and classical linear theory predictions indicates a large difference in the slopes of the two curves, which has implications for the estimation of trimmed performance values. The attainable thrust methodology does not predict an increment in pitching-moment coefficient.

The inviscid drag coefficients are examined in Fig. 14. The classical linear theory estimate is composed of wave drag due to volume plus the drag due to lift. The attainable thrust estimate sums an attainable thrust term with the classical linear theory estimates. The Euler method, of course, computes the total inviscid drag and, therefore, does not provide a breakdown of inviscid drag components. The classical linear theory computes a lower drag coefficient than the Euler method and the attainable thrust linear theory estimate is even more optimistic.

An uncambered numerical model was constructed from the high-density numerical model to estimate the volumetric wave drag and the camber drag at $C_L = 0$. The Euler code estimate of volumetric wave drag is 16.8 counts for the uncambered wing body. The inviscid drag at $C_L = 0$ is 20.6 counts for the cambered wing body; therefore, the camber drag at $C_L = 0$ is 3.8 counts.

The inviscid lift-to-drag ratio is plotted vs C_L in Fig. 15. The Euler estimate is lower than either of the linear theory estimates, which is consistent with the lift and drag coefficient predictions discussed previously. The implication of this result is that the range estimates from the aircraft design studies using linear theory would be optimistic compared to those range estimates based on Euler theory.

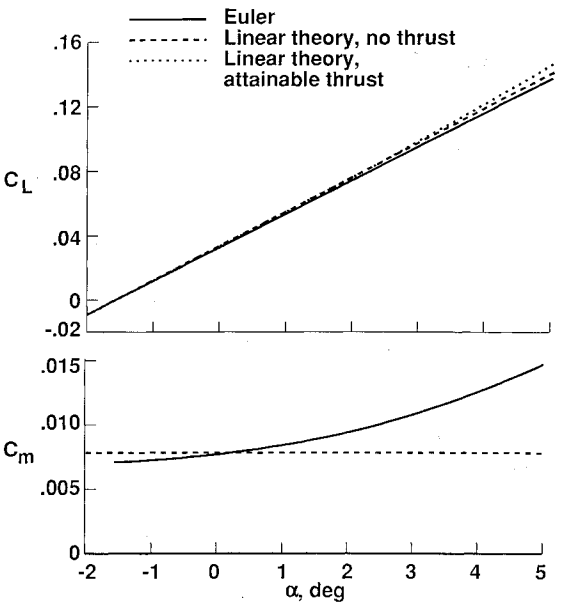

Fig. 13 Comparison of lift and pitching-moment coefficients from Euler and linear-potential theory, $M = 3.0$.

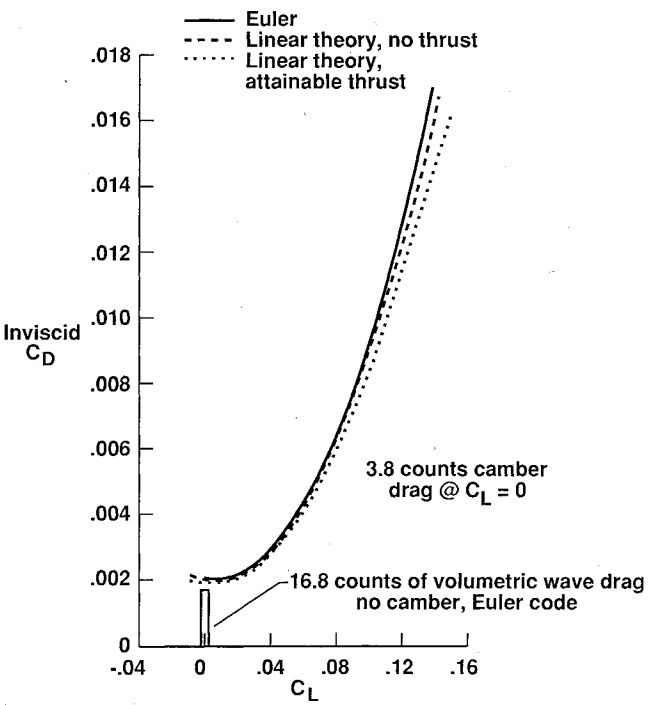

Fig. 14 Comparison of inviscid drag coefficients from Euler and linear-potential theory, $M = 3.0$.

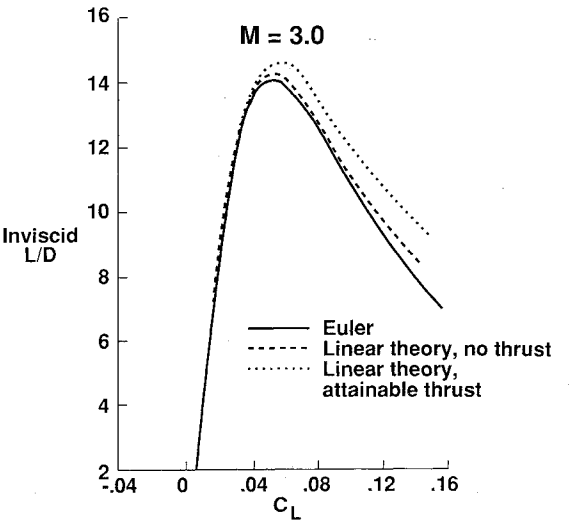

Fig. 15 Comparison of inviscid lift-to-drag ratio from Euler and linear-potential theory, $M = 3.0$.

Conclusions

A marching Euler solver, GEM3D, was used to analyze the wing body of a High-Speed Civil Transport (HSCT) concept at the cruise Mach number of 3.0. Three different grid densities, which included a variation in crossplane grid density of 61 × 42 and 97 × 58 for a nominal step size of 4 ft, or 1.5% of total length, and a variation of marching step size of 2 and 4 ft for a 61 × 42 grid, were examined to determine a suitably accurate grid. It was found that the least dense grid of 61 × 42 crossplane grid points for a 4-ft step size provided excellent flowfield resolution for roughly 11–12 min of CRAY-2 CPU time. The variation in inviscid drag coefficient compared to the more dense grids was generally 1 drag count or less for typical cruise-lift coefficients. One drag count is approximately 1% of the inviscid drag at the cruise point.

The density of the pointwise geometric description used as input to the Euler code was addressed. It was found that numerical models that are adequate for linear theory codes are too sparse for use in an Euler code and that considerable effort is required to improve a linear theory numerical input model so that an Euler solution could be obtained. An accurate representation of the nose region was found to be especially important for this particular HSCT concept, which features a blunted nose in planform. It is reiterated that a conical starting solution is an approximation for a blunted nose.

An extensive analysis of the flowfield as computed by the Euler code was performed for a typical cruise-lift coefficient of 0.1, which is obtained for $\alpha = 3$ deg. Embedded flowfield shocks on the wing upper surface were predicted, in addition to the bow shock at the nose and the wing leading-edge shock that formed on the supersonic leading-edge outer wing panel. The embedded shocks were sufficiently strong to separate a turbulent boundary layer according to a simple static-pressure criterion.

A comparison of integrated force and pitching-moment results from the Euler code and from linear theory were made at Mach 3.0. The Euler method predicted a slightly lower C_L and a slightly higher C_D compared to the linear theory, resulting in lower inviscid lift-to-drag ratios. This implies that range computations based on linear theory aerodynamic performance are optimistic compared to those based on Euler results. It was also found that there were large differences in the slopes of the pitching-moment predictions, which could have a significant impact on the sizing of control surfaces and on trimmed aerodynamic performance estimates.

This study demonstrated that an Euler method can be used to analyze the wing body of an HSCT concept and to obtain additional information on the concept that cannot be obtained

from linear theory. However, the comparisons of integrated aerodynamic quantities from both methods confirmed that linear theory is adequate for conceptual and preliminary design studies. Euler methods, as well as Navier-Stokes methods, are better suited to a more advanced design phase where the basic geometry is fixed and the emphasis is on a detailed understanding of the flowfield and/or on refinement of the geometry to improve performance.

References

[1]Colladay, R. S., "Rekindled Vision of Hypersonic Travel," *Aerospace America*, Vol. 25, No. 8, Oct. 1987, pp. 30–34.

[2]Ott, J., "High-Speed Transport Study Focuses on Lower Mach Range," *Aviation Week and Space Technology*, Vol. 128, Feb. 1988, pp. 60–61.

[3]Ott, J., "HSCT Research Defines Weight, Fuel Issues," *Aviation Week and Space Technology*, Vol. 128, March 1988, pp. 88–90.

[4]Robins, A. W., et al., "Concept Development of a Mach 3.0 High-Speed Civil Transport," NASA TM-4058, Sept. 1988.

[5]Baals, D. E., Robins, A. W., and Harris, R. V., Jr., "Aerodynamic Design Integration of Supersonic Aircraft," AIAA Paper 68-1018, Oct. 1968.

[6]Kulfan, R. M., and Sigalla, A., "Real Flow Limitations in Supersonic Airplane Design," AIAA Paper 78-147, Jan. 1978.

[7]Siclari, M. J., and del Guidice, P., "Hybrid Finite-Volume Approach to Euler Solutions for Supersonic Flows," AIAA Paper 88-0225, Jan. 1988.

[8]Craidon, C. B., "Description of a Digital Computer Program for Airplane Configuration Plots," NASA TM X-2074, Sept. 1970.

[9]Hall, J. F., Neuhart, D. H., and Walkley, K. B., "An Interactive Graphics Program for Manipulation and Display of Panel Method Geometry," NASA CR-166098, March 1983.

[10]Ames Research Staff, "Equations, Tables, and Charts for Compressible Flow," NACA Rept. 1135, Nov. 1953.

[11]Korkegi, R. H., "A Simple Correlation for Incipient Turbulent Boundary-Layer Separation Due to a Skewed Shock Wave," *AIAA Journal*, Vol. 11, Nov. 1973, pp. 1578–1579.

[12]Rose, O. J., Miller, D. S., Pittman, J. L., Ashill, P. R., and Fulker, J. L., "Full Potential Analysis of a Supersonic Delta Wing/Body," *Journal of Aircraft*, Vol. 26, March 1989, pp. 235–240.

[13]Middleton, W. D., and Lundry, J. L., "A System for Aerodynamic Design and Analysis of Supersonic Aircraft, Part 1—General Description and Theoretical Development," NASA CR-3351, Dec. 1980.

[14]Middleton, W. D., and Lundry, J. L., "A System for Aerodynamic Design and Analysis of Supersonic Aircraft, Part 2—User's Manual," NASA CR-3352, Dec. 1980.

[15]Carlson, H. W., Mack, R. J., and Barger, R. L., "Estimation of Attainable Leading-Edge Thrust for Wings at Subsonic and Supersonic Speeds," NASA TP-1500, Oct. 1979.